Bulletin of the Seismological Society of America, Vol. 93, No. 5, pp. 1984–1993, October 2003

Depth-Domain Processing of Teleseismic Receiver Functions and Generalized Three-Dimensional Imaging

by Igor B. Morozov and Kenneth G. Dueker

Abstract Stacking, either by itself or as a part of depth migration, is usually used for noise suppression in teleseismic receiver function (RF) images. However, stacking is neither the only signal enhancement method available, nor is it the most efficient in the environment of receiver-side source-generated noise typical for RF imaging. We generalize prestack depth migration methodology by introducing numerous signal-enhancement schemes in place of final summation. The method operates in full 3D, incorporates most of the existing imaging techniques, and suggests a generalized framework of RF depth imaging. We present four applications of this technique using the data from the teleseismic Continental Dynamics–Rocky Mountains teleseismic experiment: (1) building common-image gathers to assess depth focusing of RF images, (2) imaging using median and (3) coherency filters for noise suppression, and (4) generalized 3D common conversion point stacking. The results suggest that with the limited volumes and quality of the existing RF datasets, adaptive filters could be superior to record summation used in conventional depth migration.

Introduction

Teleseismic receiver functions (RFs) have become an accepted standard for imaging the crust and upper mantle discontinuities (e.g., Shearer, 1991; Bostock, 1996; Dueker and Sheehan, 1998; Shen *et al.*, 1998; Chevrot *et al.*, 1999; Gurrola and Minster, 2000). RF techniques are viewed as the primary source of detailed information on the *S*-wave velocity contrasts within the upper mantle. However, the existing RF depth imaging still lags behind its counterpart in reflection seismology, first, in the use of 2D approximations instead of 3D, and second, in the lack of approaches to help validation of image focusing. For example, although prestack RF depth migration is based on a forward *P*- to *S*-wave scattering model that is undoubtedly correct, it still does not include tools that could help determine what part of the recorded wave field actually complies with this wave propagation model. Also, it is usually assumed that record summation is adequate for extraction of the desired modes from the recorded wave field, but verification of this sufficiency presents serious difficulties with real RF data.

The existing RF imaging is based on techniques borrowed from exploration reflection seismics, such as moveout corrections, common conversion point (CCP) stacking (Dueker and Sheehan, 1998; Zhu, 2000), velocity spectrum stacking (Gurrola *et al.*, 1994; Shen *et al.*, 1998), τ-p record interpolation (Neal and Pavlis, 1999), and several types of prestack depth migration (e.g., Sheehan *et al.*, 2000; Bostock *et al.*, 2001, Bostock, 2002). However, the RF imaging environment, with limited-aperture receiver arrays or single stations, relatively sparse and uneven source distributions, and lower data redundancy and signal-to-noise ratios, is vastly different from that of exploration seismology. Consequently, reflection imaging methods also require cautious and critical modifications when applied to RF data.

We propose a general paradigm of 3D RF prestack depth migration, attained by relaxing two of its implicit assumptions. First, instead of assuming that the recorded wave field agrees with a chosen mode conversion model, we aim to provide tools that could help verify this assumption and test and enhance depth focusing. Second, we no longer assume that stacking is sufficient for attenuation of the coherent noise and allow inclusion of numerous data-dependent signal detection schemes that may be introduced by the interpreter.

With specific choices of time-to-depth mapping schemes and treatment of amplitudes, this generalized approach incorporates most of the existing methods of prestack RF depth migration or CCP stacking. Regardless of its specific type, imaging is always performed in 3D. The imaging procedure is explicitly subdivided into three steps, each of which is implemented and tested independently: (1) time-domain processing, (2) time-to-depth mapping, and (3) depth-domain processing (DDP). We emphasize extensive depth-domain analysis as the key component required for isolation of the mode of interest, as opposed to coherent and incoherent noise. Such prestack analysis is also quite practical computationally due to the relatively small volumes of RF datasets.

Multiple DDP choices lead to multiple images, and this multiplicity may seem to complicate the interpretation. However, RF depth imaging is already an inherently strongly underconstrained inverse problem, and the properties of the inversion procedures (e.g., data editing, filtering, algorithm types, and regularization) leave strong impacts on the results. For example, the results of prestack depth migration are influenced by the chosen *a priori* forward model (including assumptions of the mode content of the wave field and relative weighting of the modes), the choice of the Born versus Kirchhoff approximation (Bostock, 2002), dip filtering (Lafond and Levander, 1993), transformation of surface and emergence angle integrations into summations (Bostock *et al.*, 2001), other types of pre- and postconditioning (Chavent and Plessix, 1999), or by the choice of a single-pass migration versus iterative inversion. Underlying processing causes uncertainty of RF images that is expressed in variations of the structural types of images produced and in potential artifacts. This uncertainty may be greater than usually acknowledged and is a source of concern. In the multiprocessing approach facilitated by the DDP method, we provide means for assessment (however, still not the final judgment) of the viability of the various imaging strategies.

A serious vulnerability of conventional RF processing, particularly at frequencies above ~0.5 Hz, is the potential for imaging artifacts caused by crustal scattering (e.g., Bannister *et al.*, 1990; Gupta *et al.*, 1990; Wagner and Langston, 1992; Clouser and Langston, 1995; Abers, 1998; Revenaugh, 2000; Langston and Hammer, 2001; Bertrand *et al.*, 2002). The background of receiver-side signal-generated noise may be indistinguishable from mode conversions in the final (even stacked or migrated) image. Imaging artifacts from stacking direct and guided waves are well known in reflection seismics, and practically the only recognized way to suppress such artifacts is to identify, isolate, and attenuate them in the prestack domain (e.g., Steeples and Miller, 1998). Enhancement of such prestack analysis to RF imaging is the primary objective of the DDP method.

After an overview of the concept of the Common Image Gathers (CIGs) that is central to DDP, we describe the generalized 3D depth RF imaging method. In the following examples, we present CIGs of real RF data from the Continental Dynamics–Rocky Mountain (CD-ROM) experiment (Dueker *et al.*, 2001; Morozov and Dueker, 2003) and give three alternative CD-ROM depth images. Finally, we discuss the interpretation of these images and show that the CCP stacking can also be implemented using the new approach, with all the advantages of the generalized DDP.

CIGs in RF Imaging

For a given surface point ($\mathbf{I}_S$ in Fig. 1), a CIG is obtained simply by mapping all (or a subset of) the input time-domain RF records into depth under that point (CIG well in Fig. 1). Summation of such depth-mapped records within a CIG results in a prestack depth-migrated image under that point.

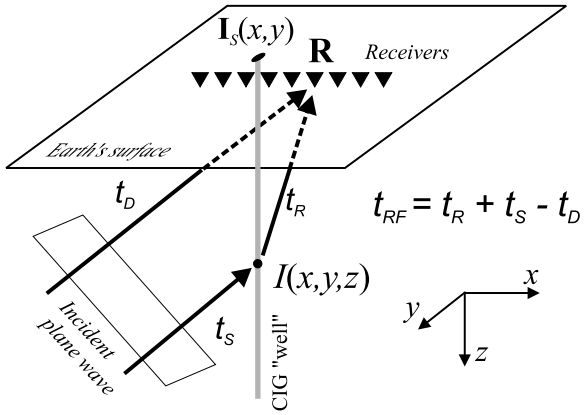

Figure 1. Time-to-depth mapping of a P_DS mode used in prestack depth migration and in the formation of the common-image gathers CIGs. For each of the incident P waves, travel times (t_S) of the surface reflection to every point within the model are precomputed and stored. For each of the receivers, **R**, the S-wave travel times to every point of the model are also precomputed. Further, for each RF record and imaging point $I(x,y,z)$, the corresponding travel-time maps are combined to form the predicted RF time, t_{RF} (x,y,z) [$t_D = t_S(\mathbf{R})$ is the time of the primary arrival]: for any surface location (x,y), the inverse of this function yields the desired mapping: $t_{RF} \rightarrow z$. The travel times are modeled in a 3D (V_P, V_S) velocity distribution (however, we used a 1D IASP91 model in this study) using an eikonal travel-time solver.

However, before (or instead of) such summation, additional useful information could be obtained from the CIG and numerous imaging techniques could be devised through CIG processing.

In exploration and crustal reflection seismics, CIGs are used for velocity analysis in prestack depth migration (Al-Yahya, 1989; Lafond and Levander, 1993). Theoretically, when displayed sorted by the source–receiver offsets, the records in a CIG show depth-offset moveouts related to errors in the background migration velocity model. In RF imaging, the ray parameter is an equivalent to the offset, and therefore event moveouts (variations of their time with p) in a CIG can be directly related to the errors in background velocities (Al-Yahya, 1989). However, in the RF case, the sensitivity of these moveouts to velocity errors is weak. For example, it can be shown that for a Pp_DS conversion from the Moho, a 10% increase of the bulk V_S of the crust (keeping V_P fixed) would result in a CIG moveout below 0.5% within the typical RF ray-parameter range. Therefore, with reasonable velocity uncertainties, all the Pp_DS events in a CIG should be always nearly horizontal, and the prevalence of strongly dipping events would indicate seismic phases that are not accounted for by the chosen mode kinematics (reverberations and shallow, broadside scattering). Similarly to Pp_DS, sensitivity of timing of other converted modes to background velocity errors is also small.

The DDP scheme analyzes and processes each of the

CIGs individually before they are assembled into a final image. In cases in which scattered events can be identified in CIGs, one could also design a filter to suppress these noise events. Processing thus becomes data and target dependent, and consequently no universal imaging recipe can be prescribed for all cases. Instead, in each particular case, one should interpret the causes of CIG event misalignments and build a DDP filter attenuating these misaligned events.

Generalized 3D Prestack Depth Migration

By including a depth signal detection step into prestack depth migration (Morozov and Levander, 2002), the latter method is extended into a broad class of RF imaging approaches. Owing to its kinematic equivalence to Born or Kirchhoff prestack depth migration (e.g., Sheehan *et al.*, 2000; Bostock *et al.*, 2001, Bostock. 2002), all the arguments in favor or against such migration hold for this approach as well; however, its full 3D formulation remains an important difference of DDP migration from the existing methods.

Recognizing the fact that seismic velocities (and hence the timing of teleseismic arrivals) are known relatively accurately but the amplitudes of RFs are often contaminated with strong receiver-end scattering noise (leading to image coherency $\ll 1$; cf. Morozov and Dueker, 2003), we compensate the predictable kinematics of the seismic phase of interest (in this case, the $P_{\mathrm{D}}S$ or $Pp_{\mathrm{D}}S$ mode conversion) and focus on the resulting event alignment (phasing). A compact formulation of this approach arises from prestack depth migration as an inverse of the following forward problem, in matrix form (e.g., Chavent and Plessix, 1999):

$$\mathbf{WU} = \mathbf{WBR}. \tag{1}$$

Here, $\mathbf{U}$ is the recorded RFs, $\mathbf{R}$ is the mode conversion amplitude of interest, $\mathbf{B}$ is the propagator (e.g., a combination of the source and receiver Green's functions), and $\mathbf{W}$ is a diagonal weight (preconditioning) matrix. For a given recording time t, the matrix product (1) is reduced to summation over the surface t = constant ("scattering ellipsoid") within the model. An important application of $\mathbf{W}$ is dip equalization, transforming the summations over the recording surface into a summation over ray directions at the imaging point (often referred to as the generalized Radon transform [cf. Beylkin and Burridge, 1990]; for recent applications to RF, see Bostock *et al.* [2001] and Bostock [2002]).

Direct and even iterative inversion of system (1) is often computationally prohibitive, and, because of high noise levels, it could also be meaningless in RF imaging. An inexpensive, one-pass approximate inverse (usually called migration) is obtained by using the backprojection operator $\mathbf{B}^T$ (T denotes the matrix transpose) multiplied by some diagonal, postconditioning matrix $\mathbf{K}$ (Chavent and Plessix, 1999):

$$\mathbf{R} = \mathbf{KB}^T\,\mathbf{W}^T\,\mathbf{WU} \equiv \sum_i \mathbf{FU}_i, \tag{2}$$

where $\mathbf{F} = \mathbf{KB}^T\mathbf{W}$. Expression (2) renders the depth image ($\mathbf{R}$) as a sum of RFs ($\mathbf{U}_i$), converted to depth, weighted (Fig. 1). Depending on the choice of $\mathbf{B}$, $\mathbf{W}$, and $\mathbf{K}$, this weighting may include amplitude corrections to compensate the geometrical spreading, uneven source-receiver distribution, and also uneven azimuthal, dip, and ray-parameter coverage of the subsurface.

The purpose of matrix $\mathbf{K}$ in equation (2) is to provide the appropriate scaling of the resulting model; one example is $\mathbf{K} = \mathrm{diag}(\mathbf{B}^T\mathbf{W}^T\mathbf{WB})^{-1}$, corresponding to the true-amplitude approximation (Chavent and Plessix, 1999). As with any underconstrained problem, there exist various choices for regularizing $\mathbf{K}$ (e.g., mass lumping; Chavent and Plessix, 1999). The data weights $\mathbf{W}$ may include obliquity and dip equalization factors; combined with the forward model $\mathbf{B}$ and regularization parameters, these factors control the tradeoff between model resolution and variance. In summary, the combined choices of operators $\mathbf{B}$, $\mathbf{K}$, and $\mathbf{W}$ yield multiple possible migration schemes, of which perhaps the most notable are a group of generalized Radon transform methods (Bostock *et al.*, 2001; Bostock, 2002).

With a large variety of possible migration approaches, elaborate inversion schemes relying on subtle amplitude correlations among the records are hardly warranted by the strong level of noise and sparse sampling of the 5D (source and receiver coordinates plus time) data space. In the following, we concentrate on the more modest task of assessing the consistency of RF phasing, and for this purpose it suffices to choose diagonal unit matrices for $\mathbf{W}$ and $\mathbf{K}$ and use a simple asymptotic approximation for $\mathbf{B}$ based on geometric ray spreading (Vidale and Houston, 1990).

For a single imaging point, the migration result (equation 2) is a sum of the input RF waveforms, transformed to depth and taken with the appropriate weights. At this point, we no longer rely on the cancellation of noise amplitudes through summation (equation 2), but replace it with a general combination of depth-mapped records:

$$\mathbf{R} = \Psi(\mathbf{FU}_1,\ \mathbf{FU}_2,\ \mathbf{FU}_3,\ldots). \tag{3}$$

This (in general) nonlinear operator Ψ can now include scaling, filtering, signal enhancement (e.g., various kinds of stacking; median, principal-component, or coherency filtering), record normalization, sorting, display, and other operations. The resulting imaging method (equation 3) can be better described in algorithmic fashion, as a depth-domain seismic processing (DDP) sequence. For every surface location $(X,\ Y)_i$,

DDP 1. map all the input RFs to depth at this location, using 3D ray kinematics ($\mathbf{FU}_i$);
DDP 2. form a section of depth-domain records $\mathbf{FU}_i$;
DDP 3. process the section obtaining one or several output records $\Psi(\ldots)$;

DDP 4. sum the resulting records $\Psi(\ldots)$ and place them at the location (X, Y) within the model.

Step DDP1 is purely model based (Fig. 1) and is carried out (provided that the background velocity structure is known) with a high degree of certainty and, most importantly, independently of the data quality. By contrast, the amplitude and phasing analysis, step DDP3, is performed within a flexible processing sequence and should combine various tools aimed at isolation of scattering artifacts and other adverse factors. Without this step, the approach represents the traditional 3D Kirchhoff prestack depth migration.

Although DDP procedure is simple and straightforward, it requires specialized program implementation that allows user-defined seismic processing flows embedded within the migration loop. Conventional RF processing methods (in particular, using Matlab) still prove cumbersome in 3D because of poor performance and computer memory utilization. We utilized an object-oriented seismic processing approach by Morozov and Smithson (1997) that has been recently expanded with tools for migration based on traveltime maps (Morozov and Levander, 2002) and for handling teleseismic records. Its modular design and run-time configuration of complex processing flows allows utilization of a number of migration weighting schemes and a dip filter controlled by the choice of parameters **B** and **W** in operators (equation 2). Similarly to commercial seismic processing systems, the entire DDP procedure is described using a specialized scripting language providing access to over a hundred seismic processing tools (Morozov and Smithson, 1997). Next we present three applications of this technique.

Real-Data Examples of Depth-Domain RF Processing

We start with two types of multichannel RF processing that provide insight into the construction of prestack RF image. We use teleseismic data from a broadband teleseismic array deployed as a part of the CD-ROM experiment from June 1999 to June 2000 (Dueker *et al.*, 2001). Of the two CDROM deployments, we choose the northern part, consisting of 21 stations spaced at about 10–12 km and straddling the Cheyenne Belt suture (Fig. 2). This is one of several relatively large and dense PASSCAL arrays operated recently, and it provides a good datasets for detailed analysis of the crust and upper mantle. Targeting the variations of lithospheric properties across the Cheyenne Belt, we placed the 3D imaging grid with horizontal and vertical spacing of 2.5 km centered under the array (Fig. 2). Although the array is nearly linear, and therefore provides usable resolution only along its axis, we performed 3D imaging to account for out-of-plane backazimuths (Fig. 1). For time-to-depth mapping, we utilized the 1D IASPEI91 model; as the sensitivity of RFs to velocity variations is relatively low, this model is sufficient for illustration of DDP techniques.

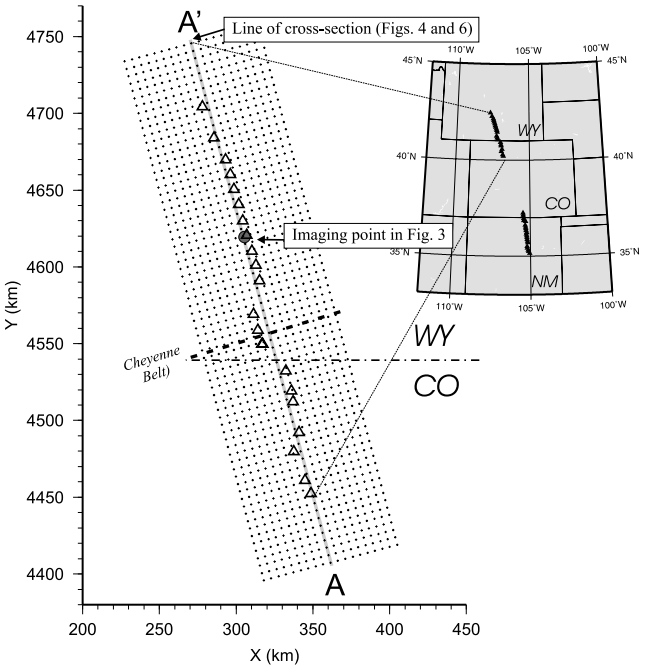

Figure 2. The northern part of the CDROM array. The approximate location of the Cheyenne Belt is shown with a thick dashed line. The rectangular imaging grid is also shown, decimated to every fourth node for clarity. The node at 50 km along the axis of the array and the line of a cross section used in the examples are highlighted in gray. Coordinates are the Universal Transverse Mercator; the inset shows the location of the entire CDROM array. Stations are triangles. WY and CO indicate the states of Wyoming and Colorado, respectively.

CIGs of Real CD-ROM RF Data

To create a CIG for a selected point of the imaging grid (Fig. 2), we performed DDP migration into that point with the DDP3 flow consisting of a trace display sorted by the absolute value of ray parameter (p). In the resulting prestack CIG section (Fig. 3), the Moho can be traced relatively unequivocally at ~40-km depth. However, below the Moho, the resulting image shows poorer coherency. Since errors in the background velocity model can account for small CIG moveouts, any misalignment of the records should be due to crustal scattering, site effects, and contributions from converted modes different from the one chosen for time-to-depth mapping. However, with relatively few records in the CIG, it is difficult to isolate noise wave trains without extensive dip filtering in the depth–ray-parameter domain. Such filtering can be applied (see the example of coherency-filtered migration), yet it also involves a danger of overprocessing.

Two conclusions can be drawn from an inspection of real-RF-data CIGs: (1) significantly larger data volumes are required for reliable imaging below the Moho (at least for this dataset), and (2) since CIG coherency is not apparent and the numbers of records in the existing datasets are lim-

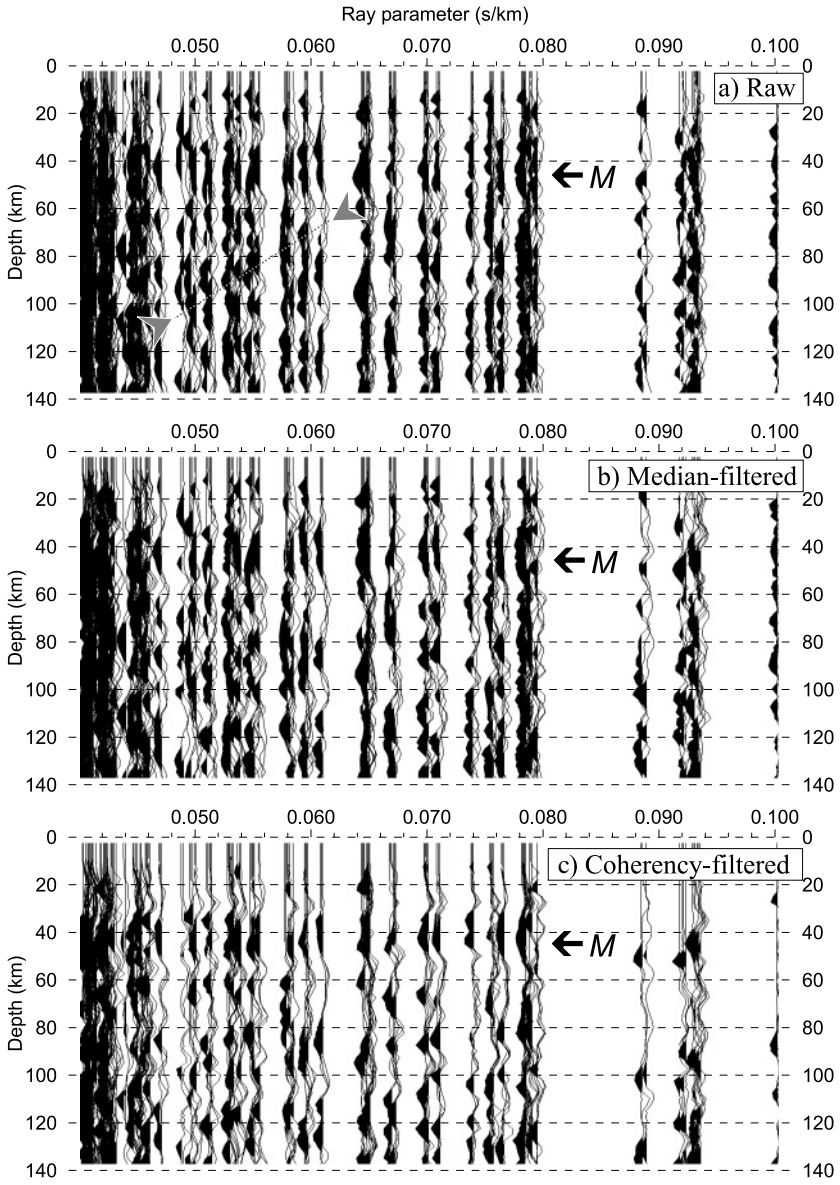

Figure 3. (a) Common image gather (CIG) for the center of the imaging grid (large gray dot in Fig. 2) after conventional processing; a stack of these records constitutes the traditional prestack depth-migrated image at the center of the array (Fig. 4, top). (b) The same CIG after median filtering within a sliding window of 20 records. (c) The same CIG processed using a slant filter enhancing all events within a range of depth moveouts between ± 2000 km/(sec km^{-1}). Note the strong nonhorizontal noise events marked with gray arrows. (d) The same CIG after application of a nonlinear slant filter designed to reject the nonhorizontal depth moveouts. These CIGs are used to build the corresponding depth-migrated images in Figure 4.

ited, robust signal detection schemes (not simply relying on record summation) are needed in order to improve imaging. In the following examples, we experiment with two possible schemes of this kind.

Generalized Prestack Depth Migration

Median filtering is broadly accepted as a statistically stable signal estimator in the background of strong noise. Its stability is due to the relative insensitivity of the median to large-amplitude outliers; by contrast, with low-fold stacking, such outliers can dominate the average.

To incorporate median filtering into depth migration, the records were sorted by the ray parameter and a sample-by-sample median filter was included in step DDP3. Although it is possible to apply a median filter to all of the records within a CIG, we chose to apply this filter within a running trace window. For each of the CIGs corresponding to the individual imaging locations (Fig. 3), a window of 20 records was arranged, moving from one end of the CIG to another. For each window position, a sample-by-sample median of the records was computed and assigned to the trace at the middle of the window (Fig. 3b).

As explained earlier, in the depth domain, we are only interested in the events with zero moveouts. Nevertheless, strong signal-generated noise and reverbs with nonzero moveouts are present in the CIGs, if not dominant (Fig. 3). Coherent noise is particularly dangerous because it will stack constructively and produce spurious events in the final image. Therefore, a better strategy for event enhancement could consist in detection of the strongest noise (nonhorizontal in the depth domain) events and in their removal from the CIGs. To detect such events, we experimented with a

coherency filter similar to that applied to reflection crustal datasets of the Canadian Lithoprobe program (Milkereit and Spencer, 1989).

For such filtering, we arranged the same sliding windows within the CIGs as before and within each of these windows computed 21 slant stacks within the range of moveouts from -2000 to 2000 km/(sec km^{-1}). For each of these moveouts, the semblance was defined as the ratio of the stack power along this moveout to the maximum stack power among all of the moveouts examined. Further, local (depth and ray-parameter dependent) coherency was defined as semblance raised to a power of $\gamma = 2$ (the typical choices for γ are 1 and 2; Milkereit and Spencer, 1989). This coherency was used as stacking weight emphasizing the strongest linear events. Finally, such events with nonzero moveouts were removed from the output of our filter. The resulting filtered CIGs (Fig. 3c) show marked differences from the unprocessed gather (Fig. 3a). The Moho stands out better throughout the entire range of ray parameters, and discontinuities below 80-km depths are more apparent (Fig. 3c).

By applying the three depth-domain filters at each surface location (Fig. 1), we obtained the corresponding migrated images (Fig. 4). We deliberately extended our imaging grid by ~40 km beyond the ends of the array (line XX′ in Fig. 2), so that migration artifacts at the ends of the array are apparent and may be compared with similar features within the section (Fig. 4). Somewhat surprisingly, the running (20-trace) median filtering resulted in a less coherent image compared to the straight stack (Fig. 4b,a, respectively). Nonlinear slant filtering resulted in the most coherent cross section (Fig. 4c).

The resulting images have many common features that appear to be robust (Fig. 5): a gap in the Moho, a step in crustal thickness across the Cheyenne Belt, and north-dipping contrasts within the mantle at 90- to 120-km depth beneath the Cheyenne Belt. However, at greater levels of detail, the migrated images in Figure 4 show significant differences. A possible approach to interpretation could thus be to identify the features that are consistent across the variety of processing choices, particularly among those using the more stringent signal detectors. (e.g., prestack coherency filtering).

CCP Stacking

CCP stacking is an established method of array RF imaging based on an approximation of horizontally layered Earth and uniform P_DS conversion amplitudes (e.g., Dueker and Sheehan, 1998; Zhu, 2000; Dueker *et al.*, 2001). Diffractions are ignored in CCP mapping, resulting in increased continuity of the image within the crust and higher horizontal detail deeper within the mantle. Theoretically, CCP stacking could be preferable when there is sufficient evidence for predominantly horizontal layering.

CCP stacking can also be rendered in the form of our DDP process with the time-to-depth mapping performed differently (Fig. 6b). Provided the background velocity is known, CCP time-to-depth mapping is controlled by the horizontal bin-sharing distance, b (Fig. 6b; Dueker and Sheehan, 1998; Zhu, 2001). For an imaging point, **I**, only RFs with their corresponding conversion (piercing) points, **C**, within distance b from **I** are considered (Fig. 6b). RF amplitudes mapped into depth at points **C** are summed yielding the CCP stack at **I**.

Figure 4d shows an axial slice through a CD-ROM 3D CCP stack computed using a bin-sharing distance of 20 km (Dueker *et al.*, 2001). Along with similar features to the migrated images (Fig. 4a–c), the two strong distinctions of the CCP stack are the spurious event at zero depth (caused by stacking of the zero-lag RF pulse corresponding to the direct P wave) and a smoother and stronger Moho, with a significantly narrower gap in the region of the Cheyenne Belt (Fig. 4). Both of these features, however, are artifacts of CCP stacking caused by a fixed horizontal bin sharing exceeding the Fresnel zone at and above the Moho depth. By contrast, migration (Fig. 4) appears to be more successful in focusing the dipping events from 90- to 120-km depth.

Discussion and Conclusions

Because of the proximity of coherent noise to useful signal, multichannel depth RF imaging differs from exploration seismology and is probably closer to shallow reflection seismics. In such an environment, special processing and interpretational efforts are required in order to avoid misinterpretation (Steeples and Miller, 1998; Morozov, unpublished data, 2003). The DDP scheme could alleviate this problem by offering a general yet standardized control of the numerous aspects of image formation by (1) providing a uniform three-step formulation encompassing many of the existing RF depth imaging techniques, (2) facilitating prestack visualization and filtering of the records in the depth domain and testing the validity of the forward model, and (3) introducing multiprocessing in order to facilitate assessment of the impact of processing and inversion on the final image.

The two most important features of the DDP framework are its inherent 3D character and explicit separation of the time-to-depth mapping from the subsequent processing in depth domain. For a given target wave-field mode, DDP is focused on a single depth point, with all the true events aligned horizontally. Such alignment simplifies coherency analysis, and a variety of filtering and processing tools could be included in this environment. The aim of such processing would be to detect and/or enhance horizontally aligned energy in a multichannel record, a relatively simple task given the vast experience in similar processing accumulated in reflection seismology. In addition to those illustrated earlier, several of potentially useful approaches of this kind include diversity stack (Embree, 1968), optimal filters (e.g., Rietsch, 1980), principal-component (Karhunen–Loève, Singular

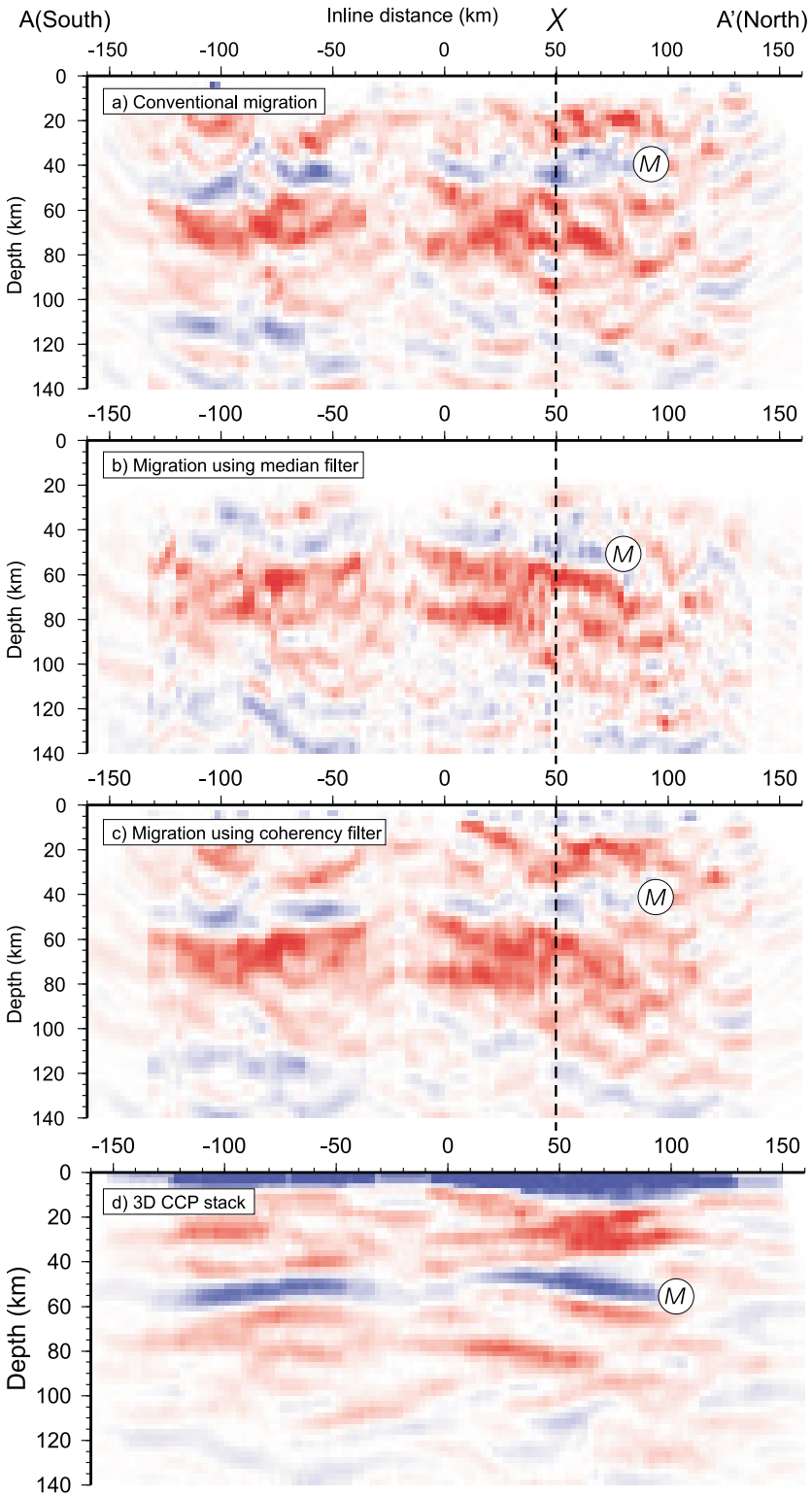

Figure 4. A slice of the migrated 3D image along the axis of the imaging grid (gray line in Fig. 2), using three different signal detection techniques illustrated in Figure 3: (a) using the diffraction-stack prestack depth migration (Fig. 3a); (b) using the same kinematics and amplitude weighing as in the migration, but applying a median filter at every depth point (Fig. 3b); and (c) using DDP migration with a built-in coherency filter rejecting the nonzero depth versus ray-parameter moveouts in the CIGs (Fig. 3d). Blue corresponds to positive and red to negative amplitudes. Note the differences in the images below the Moho (labeled M) and the different degrees of migration noise ("smiles") near the edges of the images. (d) Axial slice of 3D CCP stack (Fig. 2) obtained using the DDP method (Fig. 6; see discussion in the text). Due to conditioning by the 20-km bin sharing the Moho image is significantly more coherent than in the migrated images and most of the sub-Moho features appear subhorizontal.

Value Decomposition) filters (Hemon and Mace, 1978), sign statistic filters (Hansen *et al.*, 1988), *f-x* deconvolution, correlation autostatics, and coherency filters. DDP can also incorporate bootstrapping of the data volume (Sheehan *et al.*, 2000; Morozov and Dueker, 2003) to assess the image errors and artifacts.

Given that RF images are always conditioned by the algorithms, comparison of several imaging schemes (Fig. 4a–d) applied to the same data (and using the same 3D grid and velocity model) would provide a basis for checking their respective underlying assumptions. For example, the CCP stack shows an apparently greater continuity and amplitude

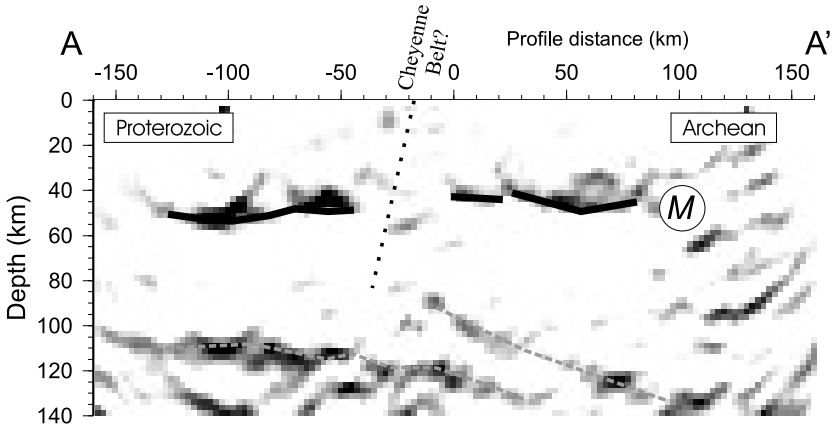

Figure 5. Interpretation of the common features of the images in Figure 4 (the image is from Fig. 4c). The different migration techniques consistently indicate the Moho (labeled M) with a gap near the Cheyenne Belt, a thicker Proterozoic crust south of it, and north-dipping structures at 90- to 120-km depth (highlighted with gray dashed lines). The projection of the Cheyenne Belt suture could be inferred from the gap in the Moho and truncation of the upper of the two mantle features, to 80- to 100-km depth. Gray shading shows only positive amplitudes.

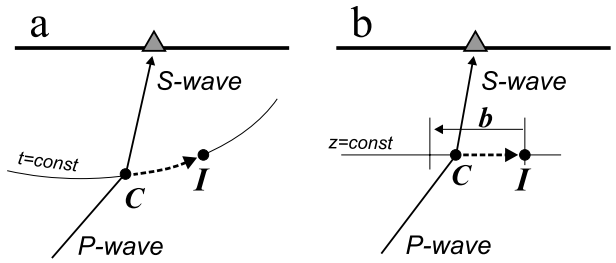

Figure 6. Comparison of the time-to-depth mapping used in (a) prestack depth migration and (b) CCP stacking. In migration, the RF amplitude at conversion point **C** is mapped into the imaging points **I** located on a scattering ellipse corresponding to a constant P_DS conversion time. In CCP stacking, a piercing point **C** is determined using station and source coordinates and assuming a horizontally layered structure. This point is migrated horizontally into the imaging points *I* located within a bin sharing distance *b* from **C**.

of the Moho and suggests several south-dipping events below about 80 km within the mantle (Fig. 4d). However, in the migrated images, this depth range is dominated by north-dipping events, at least in the northern part of the array (Fig. 4a–c). Since neither of our migration schemes includes any enhancement of lateral coherency, the appearance of these continuous events supports their authenticity.

Failure of the median-filtered migration to produce an improved image compared to the straight stack (Fig. 4b) is somewhat disconcerting. Median filtering is generally considered to be a robust approach to averaging noisy data; however, in our case, the unfiltered and coherency-filtered migrations perform better. This observation may reflect the difference between the visual appeal of the image (e.g., judged by the continuity of the boundaries) and its internal consistency, and therefore the median-filtered image may indeed indicate insufficient sampling. This problem should be alleviated with acquisition of larger data volumes.

By relaxing the emphasis on elaborate forward models and inverse solutions, the DDP method offers a simple and uniform approach to 3D imaging. Given the heterogeneity of the crust and mantle and the scattring noise levels in RF records, mapping of mantle structures should be performed in 3D (Fig. 4). Note that despite the similarity in the in-line migrated images (Fig. 4), the horizontal slices are strikingly different (Fig. 7), suggesting a 3D structure and also sampling decrease toward the edges of the 3D volume. However, a larger and true 3D dataset is required for further assessment of the properties of 3D RF imaging. When carefully implemented, generalized 3D DDP migration is also quite affordable. In our examples (Figs. 2, 4), migration of the entire dataset (~2000 RFs) took only about 15–40 min on a 2-GHz Linux PC, depending on the types of embedded filtering utilized.

Finally, the potential of DDP extends far beyond the examples presented here. Virtually any of the existing RF depth imaging schemes can be incorporated via this approach, with the advantages of 3D imaging and robust signal detection. Other types of travel-time mapping (e.g., targeting surface waves or using heterogeneous, 3D travel-time models) and plane-wave migration (Poppeliers and Pavlis, 2003) could be incorporated. Array-based methodologies for computing RFs (Li and Nábělek, 1999) could also benefit from an implementation in the depth domain. This method should also provide the means for quality control (Morozov and Dueker, 2003) and statistically robust ways to perform imaging using other signal-detection techniques yet to be explored.

Acknowledgments

We are grateful to the IRIS PASSCAL program, which made the data acquisition possible. Comments by two anonymous reviewers and the associate editor, Lorraine W. Wolf, have greatly helped in improving the manuscript. This research was supported by NSF Grant EAR99-03235. I.B.M. was also partly supported by Defense Threat Reduction Agency Grants DTRA01-01-C-0057 and DTRA01-01-C-0081.

References

Abers, G. A. (1998). Array measurements of phase used in receiver function calculations: importance of scattering, *Bull. Seism. Soc. Am.* **88,** 313–318.

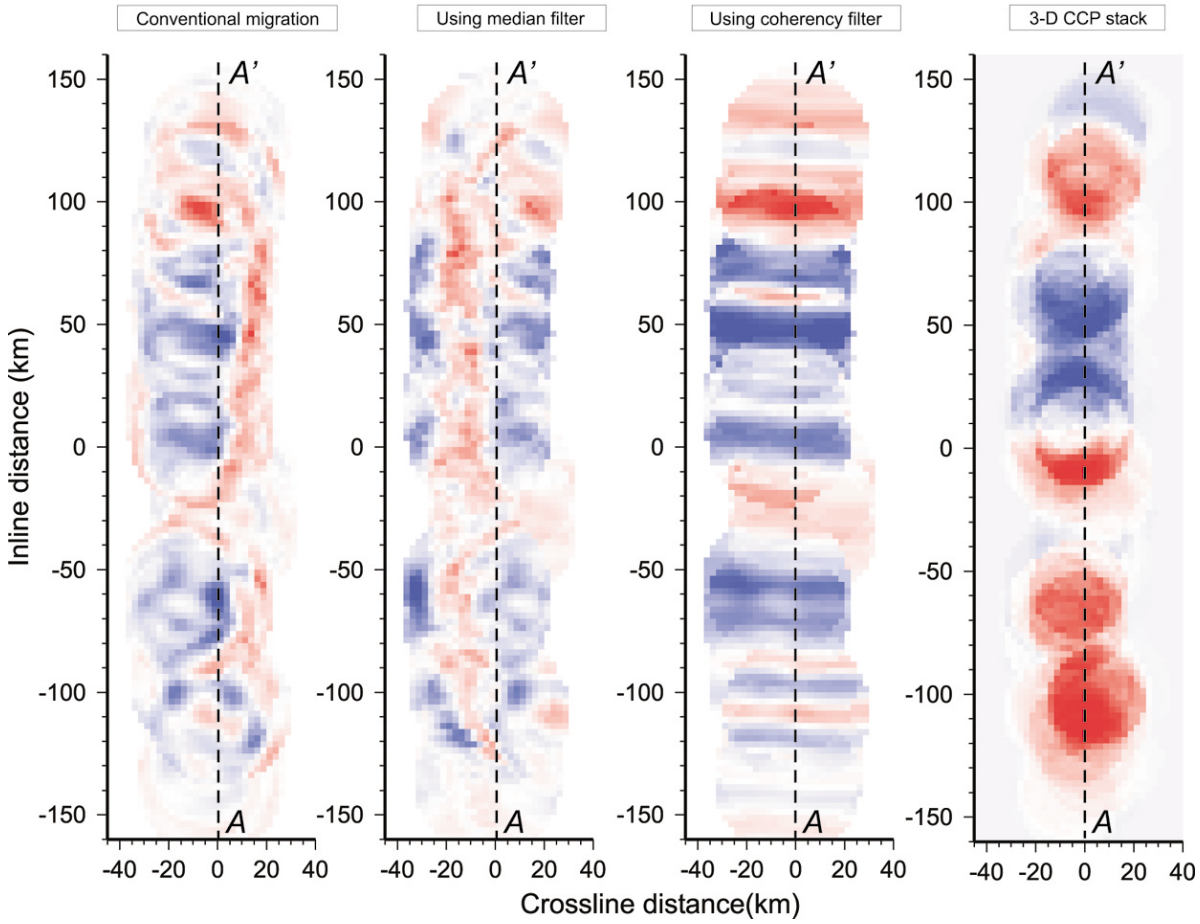

Figure 7. Horizontal slice at 45-km depth through the migrated images in Figure 4. Note the differences in the patterns of migrated and CCP images.

Al-Yahya, K. (1989). Velocity analysis by iterative profile migration, *Geophysics* **54,** 718–729.

Bannister, S. G., E. S. Husebye, and B. O. Ruud (1990). Teleseismic *P* coda analyzed by three-component and array techniques: deterministic location of topographic *P*-to-*Rg* scattering near the NORESS array, *Bull. Seism. Soc. Am.* **80,** 1969–1986.

Bertrand, E., A. Deschamps, and J. Virieux (2002). Crustal structure deduced from receiver functions via single-scattering migration, *Geophys. J. Int.* **150,** 524–541.

Beylkin, G., and R. Burridge (1990). Linearized inverse scattering problems in acoustics and elasticity, *Wave Motion* **12,** 15–52.

Bostock, M. G. (1996). *Ps* conversions from the upper mantle transition zone beneath the Canadian landmass, *J. Geophys. Res.* **101,** 8383–8402.

Bostock, M. G. (2002). Kirchhoff-approximate inversion of teleseismic wavefields, *Geophys. J. Int.* **149,** 787–795.

Bostock, M. G., S. Rondenay, and L. Shragge (2001). Multi-parameter 2-D inversion of scattered teleseismic body waves. I. Theory for oblique incidence, *J. Geophys. Res.* **106,** 30,771–30,782.

Chavent, G., and R.-E. Plessix (1999). An optimal true-amplitude least-squares depth-migration operator, *Geophysics* **64,** 508–515.

Chevrot, S., L. Vinnik, and J. P. Mintagner (1999). Global-scale analysis of the mantle *Ps* phases, *J. Geophys. Res.* **104,** 20,203–20,219.

Clouser, R. H., and G. A. Langston (1995). Modeling observed *P-Rg* conversions from isolated topographic feature near the NORESS array, *Bull. Seism. Soc. Am.* **85,** 195–211.

Dueker, K., H. Yuan, and B. Zurek (2001). Thick structured proterozoic lithosphere of the Rocky Mountain region, *GSA Today* **4,** 3–9.

Dueker, K. G., and A. F. Sheehan (1998). Mantle discontinuity structure beneath the Colorado Rocky Mountains and High Plains, *J. Geophys. Res.* **103,** 7153–7169.

Embree, P. (1968). Diversity seismic record stacking method and system, U.S. Patent 3,398,396.

Gupta, I. N., C. S. Lynnes, T. W. McElfresh, and R. A. Wagner (1990). *F-K* analysis of NORESS array and single-station data to identify sources of near-receiver and near-source scattering, *Bull. Seism. Soc. Am.* **80,** 2227–2241.

Gurrola, H., and J. B. Minster (2000). Evidence for local variations in the depth to the 410-km discontinuity beneath Albuquerque, New Mexico, *J. Geophys. Res.* **105,** 10,847–10,856.

Gurrola, H., J. B. Minster, and T. Owens (1994). The use of velocity spectrum for stacking receiver functions and imaging upper mantle discontinuities, *Geophys. J. Int.* **117,** 427–440.

Hansen, K. M., R.-C. Chowbury, and R. A. Phinney (1988). The sign filter for seismic event detection, *Geophysics* **55,** 1024–1033.

Hemon, C. H., and D. Mace (1978). Use of Karhunen–Loeve transformation in seismic data processing, *Geophys. Prosp.* **26,** 600–606.

Langston, C. A., and K. Hammer (2001). The vertical component *P*-wave receiver function, *Bull. Seism. Soc. Am.* **91,** 1805–1819.

Lafond, C. F., and A. Levander (1993). Migration moveout analysis and depth focusing, *Geophysics* **58,** 91–100.

Li, X., and J. L. Nábělek (1999). Deconvolution of teleseismic body waves

for enhancing structure beneath a seismometer array, *Bull. Seism. Soc. Am.* **89,** 190–201.

Milkereit, B., and C. Spencer (1989). Noise suppression and coherency enhancement of seismic data, in Statistical Application in the Earth Sciences, F. P. Bonham-Carter (Editor), Geological Survey of Canada, Ottawa, Ontario, Paper 89-9, 243–248.

Morozov, I. B., and K. G. Dueker (2003). Signal-to-noise ratios of teleseismic receiver functions and effectiveness of stacking for their enhancement, *J. Geophys. Res.* **108,** no. B2, 2106 doi 10.1029/2001 JB001692.

Morozov, I. B., and A. Levander (2002). Depth image focusing in traveltime map based wide-angle migration, *Geophysics* **67,** 1903–1912.

Morozov, I. B., and S. B. Smithson (1997). A new system for multicomponent seismic processing, *Comput. Geosci.* **23,** 689–696.

Neal, S. L., and G. L. Pavlis (1999). Imaging *P*-to-*S* conversions with multichannel receiver functions, *Geophys. Res. Lett.* **26,** 2581–2584.

Poppeliers, C., and G. L. Pavlis, (2003). Three-dimensional, prestack, plane-wave migration of teleseismic *P*-to-*S* converted phases. I. Theory, *J. Geophys. Res.* **108,** no. B2, 2112 doi 10.1029/2001JB000216

Revenaugh, J. (2000). The relation of crustal scattering to seismicity in Southern California, *J. Geophys. Res.* **105,** 25,403–25,422.

Rietsch, E. (1980). Estimation of the signal-to-noise ratio of seismic data with an application to stacking, *Geophys. Prospect.* **28,** 531–550.

Shearer, P. M. (1991). Constraints on upper mantle discontinuities from observations of long-period reflected and converted phases, *J. Geophys. Res.* **96,** 18,147–18,182.

Sheehan, A. F., P. Shearer, H. J. Gilbert, and K. G. Dueker (2000). Seismic migration processing of *P-SV* converted phases for mantle discontinuity structure beneath the Snake River Plain, western United States, *J. Geophys. Res.* **105,** 19,055–19,065.

Shen, Y., S. C. Solomon, I. T. Byarnason, and C. J. Wolfe (1998). Seismic evidence for a lower-mantle origin of the Iceland Plume, *Nature* **395,** 62–65.

Steeples, D. W., and R. D. Miller (1998). Avoiding pitfalls in shallow seismic reflection surveys, *Geophysics* **63,** 1213–1224.

Vidale, J. E., and H. Houston (1990). Rapid calculation of seismic amplitudes, *Geophysics* **55,** 1504–1507.

Wagner, R. A., and G. A. Langston (1992). Body-to-surface wave scattered energy in teleseismic coda observed at the NORESS seismic array, *Bull. Seism. Soc. Am.* **82,** 2126–2138.

Zhu, L. (2000). Crustal structure across the San Andreas Fault, Southern California, from teleseismic converted waves, *Earth Planet. Sci. Lett.* **179,** 183–190.

Department of Geological Sciences
University of Saskatchewan
Saskatoon, SK S7N 5E2, Canada
(I.B.M.)

Department of Geology and Geophysics
University of Wyoming
Laramie, WY 82071
(K.G.D.)

Manuscript received 26 February 2002.